

# Collaborative Surgical Robots

## *Optical Tracking During Endovascular Operations*

© PHOTOCREDIT

By Christoff M. Heunis, Beatriz Farola Barata, Guilherme Phillips Furtado, and Sarthak Misra

**E**ndovascular interventions usually require meticulous handling of surgical instruments and constant monitoring of the operating room workspace. To address these challenges, robotic-assisted technologies and tracking techniques are increasingly being developed. Specifically, the limited workspace and potential for a collision between the robot and surrounding dynamic obstacles are important aspects that need to be considered. This article presents a navigation system developed to assist clinicians with the magnetic actuation of endovascular catheters using multiple surgical robots. We demonstrate the actuation of a magnetic catheter in an experimental arterial testbed with dynamic obstacles. The motions and trajectory planning of two six degrees of freedom (6-DoF) robotic arms are established through passive marker-guided motion planning. We achieve an overall 3D tracking accuracy of  $2.3 \pm 0.6$  mm for experiments involving dynamic obstacles. We conclude that integrating multiple

optical trackers with the online planning of two serial-link manipulators is useful to support the treatment of endovascular diseases and aid clinicians during interventions.

### **Benefits and Drawbacks to Surgical Robots**

Ever since the first documented robot-assisted surgical intervention in 1985, the field of surgical robotics has expanded in revolutionary ways [1]. In particular, surgical robots have been incorporated within the field of endovascular surgery to offer a lower-risk alternative to open operations, assist with localizing diseases, and expedite the planning of endovascular interventions. During robot-assisted procedures, serial-link manipulators may provide aid to a clinician by maneuvering cameras, lights, and medical instruments. Studies have shown that these surgeries result in shorter hospital stays, fewer incisions, and higher precision when compared to traditional interventions [2]. As attractive as robotic surgery is, there are several limitations inherent in robots, even if the machines reduce the physical burden of a clinician. Since clinicians are meticulously trained to handle surgical instruments, dealing with robots may cause them to lose both their natural

Digital Object Identifier 10.1109/MRA.2020.2976300

Date of current version: 19 March 2020

hand–eye coordination and dexterity for grasping and manipulating multiple surgical tools and instruments [3]. These drawbacks reduce both their sensory perception and situational awareness [4].

To resolve dexterity issues and improve control of surgical instruments, a magnetic-actuation approach has shown potential for diagnostic and therapeutic purposes [5]. Based on this notion, we have proposed the Advanced Robotics for Magnetic Manipulation (ARMM) system (Figure 1), which is designed to magnetically steer flexible surgical instruments, such as endovascular catheters, in a large dexterous workspace [6]. Nevertheless, some issues remain unexplored in this system. It employs two collaborative robots aimed at manipulating surgical instruments and imaging tools. However, due to the dynamic and unstructured environment in an operating room, autonomously collaborating with the robots can be challenging since it requires an effective tracking scheme. In addition, the loss of visual surgical-tool tracking is reputed to be one of the biggest impediments to the widespread use of autonomous surgical robots [7]. Consequently, the field is far from maturity, and the benefits of surgical robots are still a subject of debate in medical communities.

### Tracking in an Operating Room

Most surgical robotic systems are premised on human–machine collaboration akin to master–slave systems. Such conventional systems have employed both optical tracking [8]–[10] and electromagnetic tracking techniques (EMTs) in the operating room [11]. However, due to a clustered operating environment and small capture volumes, large tracking errors ( $\geq 4$  mm) have been reported for EMT [12]. Moreover, from the perspective of a magnetic-actuation system, these trackers are susceptible to distortions induced by ferromagnetic materials in surgical tools and electromagnets [13]. One of the most common devices for optical tracking in a clinical setting is the Northern Digital Inc. (NDI) Polaris system (Polaris Industries, Medina, Minnesota). It has been used in commercial systems such as the Da Vinci Robot (Intuitive Surgical, Sunnyvale, California) [14] and the haptic-centered Robotic Arm Interactive Orthopedic System (MAKO Surgical, Fort Lauderdale, Florida) [15] as well as in clinical studies: Nguyen et al. [9] examined the optimization of an operating room, combined with optical

constraints from an NDI system. Kengott et al. [10] investigated the use of the same tracking system for visualizing surgical instruments in relation to anatomic structures [10]. However, these studies demonstrate control by calculating the path of the instrument before the intervention (i.e., offline), which has some caveats. First, it is not robust enough for a rapidly changing environment and real-time disruptions. Next, limited information is available in advance about the environment and its dynamics. Furthermore, the NDI system has a low capture volume, confines the movement of surgical staff and equipment, and is difficult to position optimally within a clinical environment.

### Contributions

In this article, we investigate accurate preoperative planning to improve an intervention's workflow and show that real-time intraoperative planning can reduce disruptions. We propose a robotic surgical system that uses optical tracking and an online automated control system to address the aforementioned limitations. In our system, eight cameras are employed in a larger capture volume, as opposed to the conventional stereo-camera solution. We address problems related to the autonomous handling of surgical instruments and collaboration with a user in an environment that represents an operating room in the context of an

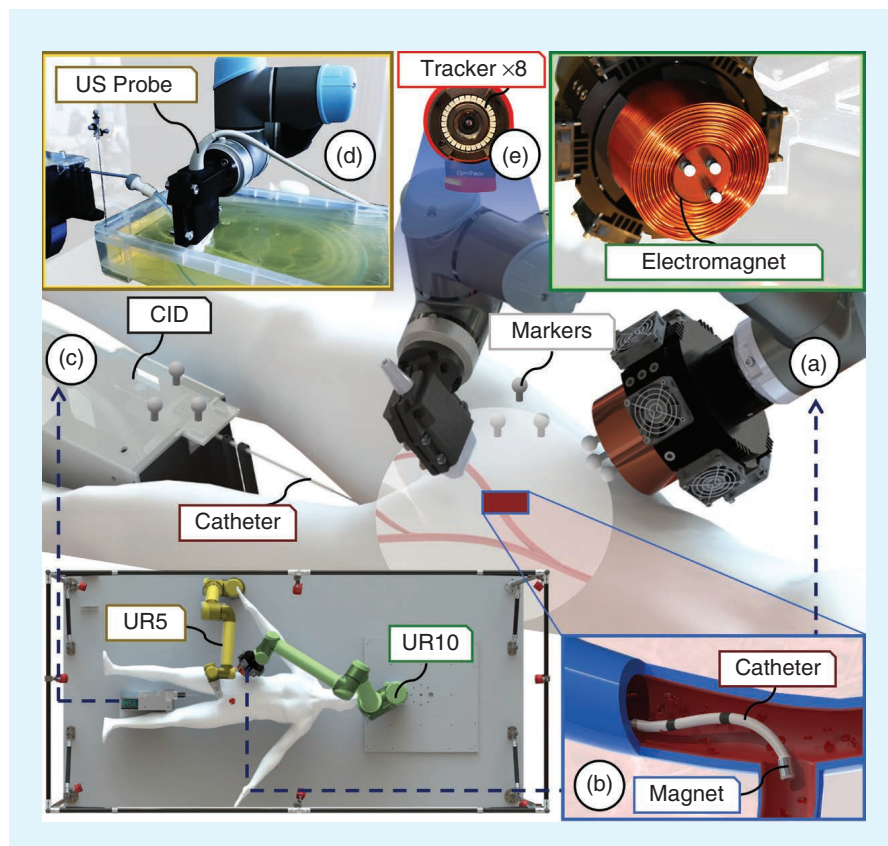


**Figure 1.** The ARMM system incorporates two serial-link manipulators. (a) One actuates an electromagnet for (b) the purpose of guiding a magnetic endovascular catheter using (c) an automated CID. (d) Another manipulator maneuvers a US transducer for intraoperative US imaging. (e) Optical tracking is used to note the pose and movement of static and dynamic objects by means of reflective markers.

endovascular intervention. Finally, we present a combined tracking and navigation system for a surgical instrument and robot arms in combination with a magnetic-actuation system that includes a real-time obstacle avoidance strategy.

### Optical Tracking in the ARMM System

ARMM consists of several subsystems (Figure 1), one of which is a cored EM coil attached to a 6-DoF robotic arm (UR10, Universal Robots, Odense, Denmark). The system includes a second robotic arm (UR5) that is capable of guiding an ultrasound (US) transducer (SonixTouch Q+, BK Medical, Peabody, Massachusetts). Additionally, it employs an efficient vision-based 3D tracking system and an automated catheter-insertion device (CID). Other details of the magnetic subsystem are discussed in our previous work [6]. In this section, we discuss the methods for setting up the cameras in the ARMM system workspace so that it represents a clinical environment.

### Preoperative Planning: Workspace Registration

We have partial information about obstacles before the motion of the robots. Therefore, to realize online planning for the serial-link manipulators and visualization of

these obstacles, the workspace must be registered preoperatively. Eight infrared cameras (Flex13, Optitrack, Corvallis, Oregon) are mounted on a truss structure that surrounds the ARMM workspace (Figure 1). Each camera has a horizontal field of view (FoV) of  $56^\circ$  and a vertical FoV of  $46^\circ$  (Figure 2). To fully utilize this capture coverage, the optimized camera placement is chosen so that points are maximally visible, with minimal 3D reconstruction error in the presence of dynamic occlusion [16]. Furthermore, tracked markers can be simultaneously recorded by at least two synchronized cameras in a capture volume of  $9 \text{ m}^3$ .

The cameras are first calibrated within the workspace reference frame ( $\{O\}$ ) using commercial calibration tools (CWM-250 Calibration Wand and Motive 2.1 L-Frame, Optitrack, Corvallis, Oregon). Next, we position a custom-made calibration tool on the UR10 end effector and move it toward 20 reference points inside the ARMM workspace. By triangulating the markers in frame ( $\{O\}$ ) in conjunction with the UR10 end-effector set point, the homogeneous transformation  $[\mathbf{T}_O^G \in \text{SE}(3)]$  can be derived that maps camera coordinates to the global reference frame ( $\{G\}$ ). This is calculated as

$$\mathbf{T}_i^j = \begin{bmatrix} \mathbf{R}_i^j & \mathbf{p}_i^j \\ \mathbf{0}_{1 \times 3} & 1 \end{bmatrix} \in \text{SE}(3), \quad (1)$$

where  $\mathbf{R}_i^j \in \text{SO}(3)$  describes the relative orientation of a frame ( $j$ ) with respect to another frame ( $i$ ), and  $\mathbf{p}_i^j \in \mathbb{R}^3$  is the translation vector from point  $i$  to  $j$ . The translation component of all position coordinates from the cameras to the global reference frame is experimentally determined by calculating the residual error between the tracked marker and UR10 set points. Based on the postcalibration results, the tracking system's mean reprojection error is 0.20 mm. The effective workspace of the ARMM system for magnetic actuation can be approximated as a hemisphere with a radius of 1,300 mm [6]. Combining this workspace with the capture volume of the tracking system ensures a well-monitored robotic setup that is applicable for use in an operating room. The functionalities of the tracking system are accessed using a software development kit from Motive (NaturalPoint, Corvallis, Oregon).

### Registering Obstacles in the Workspace

To autonomously control the ARMM manipulators, all objects within the workspace, such as the tool center point (TCP) of a manipulator, surgical instruments, the CID, and the moving hand of a clinician, should be registered. The tracking system can trace rigid body tools that have reflective markers [Figure 3(a)]. We place these markers preoperatively on objects, assuming that the best line-of-sight scenario [Figure 3(b)] involves a corner position on the top surface of the objects within the ARMM workspace [Figure 3(c)]. A user can approximate this location as the 3D position on the object farthest from the origin of the global reference frame ( $\{G\}$ ). In the case of a nonmanufactured object, such as a

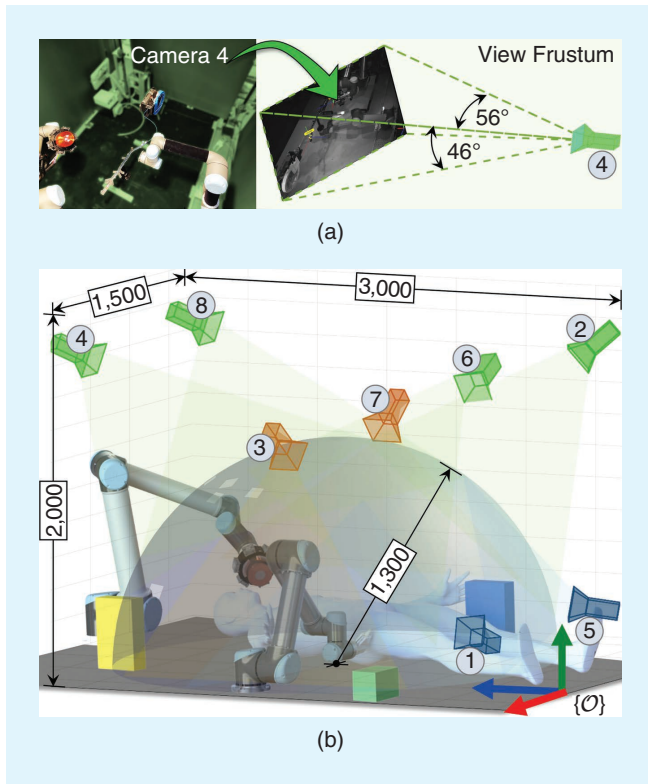


**Figure 2.** In a clinical environment, the cameras can be placed around the patient and registered in the reference frame ( $\{O\}$ ). (a) A sample image of the system workspace and the view frustum of camera ④. (b) The operable workspace for both manipulators is indicated by the hemisphere. To ensure the visualization of the patient, cameras ① and ⑤ are mounted near the workspace at ground level. Cameras ③ and ⑦ ensure the constant tracking of the manipulators. Finally, the entire workspace is visualized by cameras ②, ④, ⑥, and ⑧. All dimensions are in millimeters.

clinician's hand, this position can be chosen as a center point. Next, objects are enveloped by oriented bounding boxes (OBBs), and safety spheres are generated with respect to the relative positions ( $\mathbf{p}_o \in \mathbb{R}^3$ ) defined during the preoperative phase. Once an object is registered, a real-time visualization of its OBB is shown. Static objects require only a single registration, while dynamic (moving) objects are registered using unique and fixed rigid bodies. Each OBB contains known vertex positions connected by edges to form a cuboid shape

that is extruded toward the global origin. With the workspace and global reference frames, we specify the reference frame of the electromagnetic (EM) coil ( $\{C\}$ ), as indicated in Figure 3(c).

### Robot Navigation During Endovascular Interventions

In this section, we provide the ARMM system's control algorithms in the context of optical tracking within a clinical

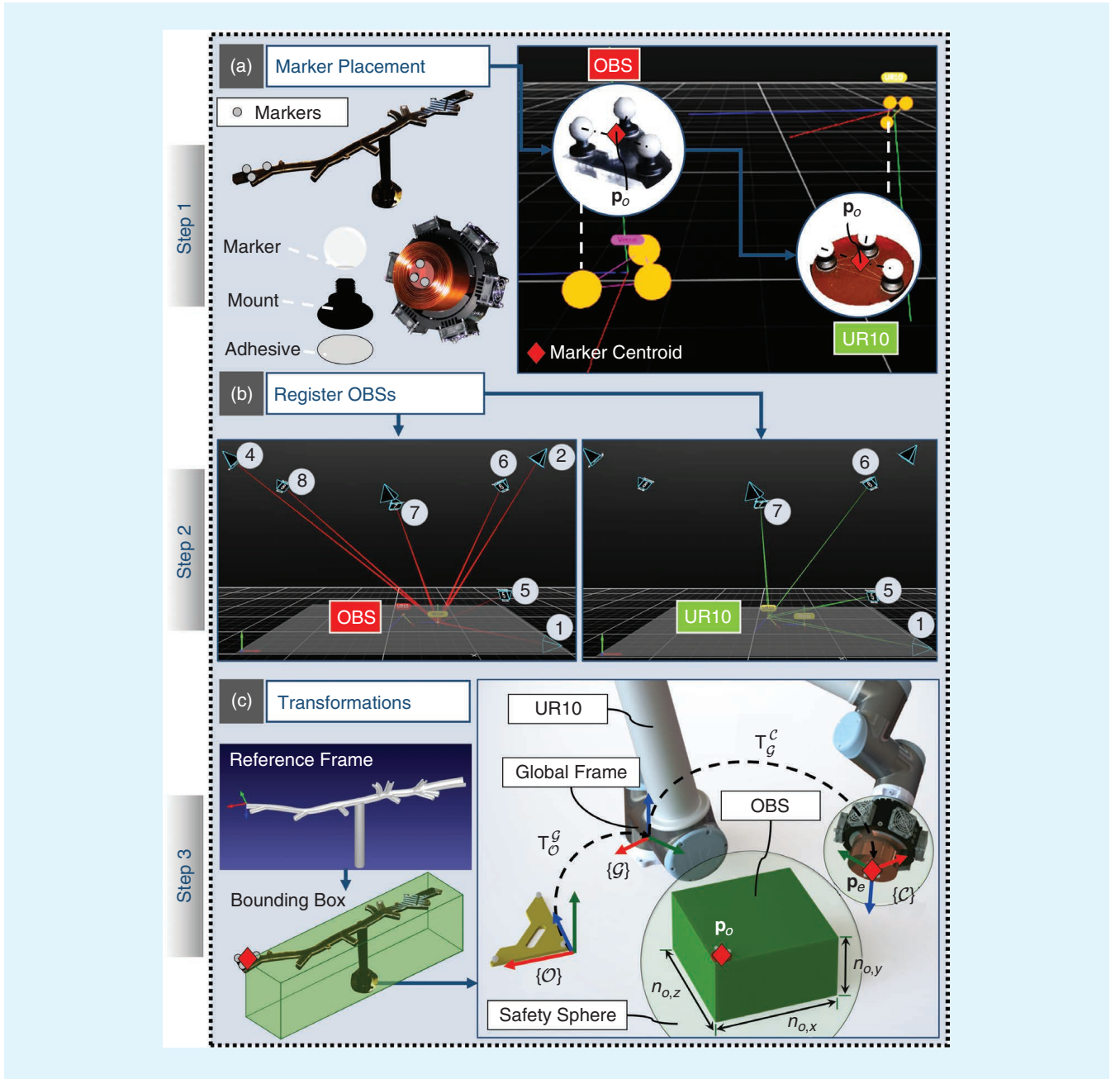


**Figure 3.** Preoperative planning occurs in three steps. (a) Step 1: Markers are registered by the tracking system as a position ( $\mathbf{P}_o$ ) after being placed at approximately the farthest 3D coordinates of the object from the origin of frame ( $\{G\}$ ). Each object is labeled with a unique identifier, e.g., "OBS" for an obstacle or "UR10" for the manipulator. (b) Step 2: Each object requires a direct line of sight from at least two cameras. The example shows seven cameras tracking the OBS and four cameras tracking the manipulator simultaneously. (c) Step 3: Using (1), we derive the transformation of the coordinates of an object with bounding dimensions ( $n_{o,x} \times n_{o,y} \times n_{o,z}$ ). The first transformation ( $T_o^g$ ) is from ( $\{O\}$ ) to ( $\{G\}$ ). The manipulator's TCP position ( $\mathbf{P}_e$ ) is derived by a second transformation ( $T_e^c$ ) that maps the coordinates to the tool frame ( $\{C\}$ ). The BB dimensions are constructed in the direction of the origin of  $\{G\}$ , and safety spheres envelope objects around their centroids.

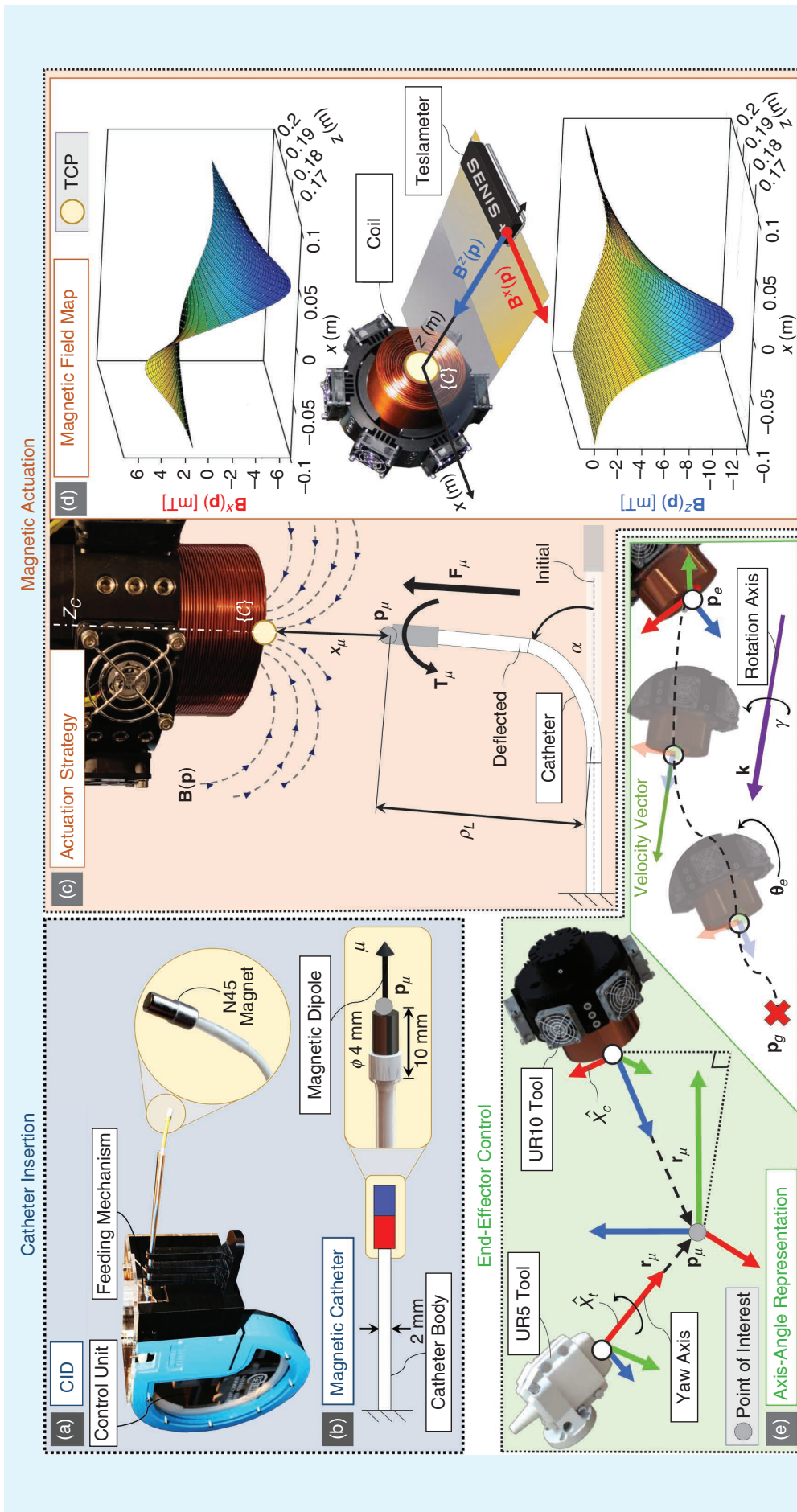


**Figure 4.** The system apparatus. (a) A CID can continuously feed or retract catheters with sizes ranging from 3 to 34 French into the port of entry, such as an incision in the groin. The body of the catheter is gripped between a gear and a bearing structure and fed through a tube by an MX-64AR Dynamixel servo motor (Robotis, Seoul, South Korea) with a 0.088° resolution at an insertion error of 0.47%. (b) An endovascular catheter is embedded with an N45 neodymium magnet (diameter: 4 mm; length: 10 mm) at its tip. The catheter is equipped with a magnetic dipole ( $\mu$ ) at position ( $p_\mu$ ). (c) The magnetic-actuation strategy employed in the ARMM system uses a mobile electromagnet to deflect the catheter by generating a magnetic field,  $[B(p)]$ . When exposed to this field at a distance ( $x_\mu$ ) from the electromagnet, the catheter tip experiences a magnetic force ( $F_\mu$ ) and torque ( $T_\mu$ ). The distal segment ( $\rho_L$ ) is then deflected to an angle ( $\alpha$ ) to align with the electromagnet axis of symmetry ( $z_c$ ). (d) Current-to-field maps are generated at a coil current of 1 A. The graphs show the magnetic field  $[B(p)]$ , where \* denotes magnetic-field magnitudes along the  $xz$  coordinates of a 2D plane with reference to frame ( $\{C\}$ ), on which the catheter should be deflected. (e) Before approximately arriving at a target position ( $p_e \approx p_g$ ), a distance vector ( $r_\mu$ ) is calculated. The end-effector orientation ( $\theta_e$ ) is adjusted so that the electromagnet axis of symmetry aligns with the distance vector. This is done by choosing an appropriate axis for  $k$  [for instance, the electromagnet  $x$ -axis ( $x_c$ )] and rotating it with a required angle ( $\gamma$ ) using (2). mt: millitesla.

environment. First, we describe intraoperative planning, which includes a magnetic-actuation strategy that specifies the manipulator trajectories, and modeling the ARMM apparatus (Figure 4). This is followed by a discussion of intraoperative control, which includes an explanation of our online control strategy.

### EM-Field Strength

To magnetically actuate an instrument, the ARMM system requires knowledge of the UR10 end-effector pose, the magnetic field ( $\mathbf{B}(\mathbf{p}) \in \mathbb{R}^3$ ) generated by the EM coil, and the location ( $\mathbf{p} = \mathbf{p}_\mu$ ) of the magnetic dipole ( $\boldsymbol{\mu} \in \mathbb{R}^3$ ) attached to the instrument [Figure 4(b)]. According to the dipole approximation, the magnetic dipole experiences a wrench ( $\mathbf{W}_\mu \in \mathbb{R}^6$ ) when exposed to an external magnetic field [17]. This wrench consists of force ( $\mathbf{F}_\mu \in \mathbb{R}^3$ ) and torque ( $\mathbf{T}_\mu \in \mathbb{R}^3$ ) components, defined as

$$\mathbf{W}_\mu = \begin{bmatrix} \mathbf{F}_\mu \\ \mathbf{T}_\mu \end{bmatrix} = \begin{bmatrix} \nabla(\boldsymbol{\mu}^T \mathbf{B}(\mathbf{p}_\mu)) \\ S(\boldsymbol{\mu}) \mathbf{B}(\mathbf{p}_\mu) \end{bmatrix}, \quad (2)$$

where  $S(\boldsymbol{\mu})$  denotes a skew-symmetric form of  $\boldsymbol{\mu}$ . Our actuation strategy [Figure 4(c)] is to orient the electromagnet so that  $\mathbf{p}_\mu$  is coincident with the coil-symmetry axis ( $\mathbf{Z}_C \in \mathbb{R}^3 : \|\mathbf{Z}_C\| = 1$ ) at all times [6]. Consequently, we can express the magnetic field at  $\mathbf{p}_\mu$  as

$$\mathbf{B}(\mathbf{p}_\mu, I) = \mathbf{Z}_C B(x_\mu, I), \quad (3)$$

where  $I \in \mathbb{R}$  is the current input to the coil,  $x_\mu \in \mathbb{R}^+$  is the distance from the dipole to the face of the electromagnet, and  $B(x_\mu, I)$  is the scalar value of the magnetic field along the coil-symmetry axis.

The electromagnet should be able to generate sufficient fields to manipulate autonomously operated catheters. Since the electromagnet is positioned outside the human body in a clinical scenario, we assume that the catheter at any instance during the procedure is located no further than 20 cm away from the electromagnet. Therefore, to obtain a current-to-field map, we experimentally measure the field using a calibrated three-axis teslameter (3MH3A-500MT, Senis, Baar, Switzerland). Throughout this task, we exploit the coil's axial symmetry [17], measuring the values in a region of the coil's  $xz$  plane [Figure 4(d)]. The measurement data are then preprocessed using an R implementation of the local polynomial surface-smoothing regression. The preprocessed data are fit using a fifth-order polynomial function. We obtain a root-mean-square error (RMSE) between the measured and fitted fields of 1.35 mT, with an average relative error of 2.34%.

### End-Effector Pose Commands

We define intraoperative planning as the phase between the offline preoperative phase and the online strategy. During intraoperative

planning, we provide a manipulator end effector's final poses to coordinate the manipulator tool frame's motions, corresponding to any activated tasks, for instance, orienting the electromagnet, inserting a needle, or actuating a US transducer. Let us consider the end-effector pose of a single robot, expressed as a position ( $\mathbf{p}_e \in \mathbb{R}^3$ ) and axis-angle orientation ( $\boldsymbol{\theta}_e \in \mathbb{S}^3$ ). Deriving the pose depends on the current manipulator TCP, its frame of reference, a distance vector ( $\mathbf{r}_\mu \in \mathbb{R}^3$ ) to a point of interest, and a unit vector ( $\mathbf{k} \in \mathbb{R}^3$ ) [Figure 4(e)]. The unit vector describes an axis of rotation, and an angle ( $\gamma \in \mathbb{R}^+$ ) describes the rotation about that axis. For example, if the distal segment of the catheter has to be deflected so that it aligns with a target vector in 3D ( $\mathbf{r}_\mu$ ), a target point for the electromagnet TCP ( $\mathbf{p}_g \in \mathbb{R}^3$ ) is chosen to lie on that vector. Furthermore, since the coil's  $z$ -axis should align with  $\mathbf{r}_\mu$  on a 2D plane, we choose its  $x$ -axis ( $\hat{X}_c$ ) to be the unit vector. The axis-angle orientation ( $\boldsymbol{\theta}_e$ ) is then calculated using the Rodrigues formula [18]:

$$\boldsymbol{\theta}_e = \mathbf{r}_\mu \cos(\gamma) + (\mathbf{k} \times \mathbf{r}_\mu) \sin(\gamma) + \mathbf{k}(\mathbf{k} \cdot \mathbf{r}_\mu)(1 - \cos(\gamma)). \quad (4)$$

Depending on the orientation of the tool reference frame, the vector obtained in (2) must be transformed using (1). This strategy can be employed using more complex end-effector tools (such as the US transducer) that require different robotic poses, as detailed in [19].

### Model-Based Trajectory Planning

A tracking thread (Algorithm 1) is implemented to continuously reconstruct obstacle vertices at a speed of 120 Hz. A

#### Algorithm 1: Generating and tracking obstacle (OBS) vertices

##### Inputs:

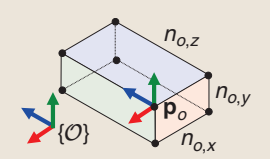
- $\mathbf{p}_o \in \mathbb{R}^3$   $\Leftrightarrow$  Corner position of the OBS [ $p_{o,x}$   $p_{o,y}$   $p_{o,z}$ ]
- $\mathbf{n}_o \in \mathbb{R}^3$   $\Leftrightarrow$  OBS-dimensions vector [ $n_{o,x}$   $n_{o,y}$   $n_{o,z}$ ]
- $\mathbf{T}_o^g \in \text{SE}(3)$   $\Leftrightarrow$  Transformation matrix from frame  $\{O\}$  to frame  $\{G\}$

##### Outputs:

- $\mathbf{n}_m \in \mathbb{R}^{8 \times 3}$   $\Leftrightarrow$  Real-time BB coordinates in  $\{G\}$

##### Tracking thread:

- 1 Track OBS position ( $\mathbf{p}_o$ ) using the motion trackers
- 2 Create an OBB to envelope the OBS

$$\mathbf{n}_n \leftarrow \begin{bmatrix} p_{o,x} & p_{o,y} & p_{o,z} \\ p_{o,x} & p_{o,y} & p_{o,z} + n_{o,z} \\ p_{o,x} - n_{o,x} & p_{o,y} & p_{o,z} + n_{o,z} \\ p_{o,x} - n_{o,x} & p_{o,y} & p_{o,z} \\ p_{o,x} & p_{o,y} - n_{o,y} & p_{o,z} \\ p_{o,x} & p_{o,y} - n_{o,y} & p_{o,z} + n_{o,z} \\ p_{o,x} - n_{o,x} & p_{o,y} - n_{o,y} & p_{o,z} + n_{o,z} \\ p_{o,x} - n_{o,x} & p_{o,y} & p_{o,z} \end{bmatrix} \quad \Leftrightarrow \text{Vertex positions for OBB stored in } \mathbf{n}_n$$


##### for $k := 1$ to 8, do

- $\mathbf{n}_t \leftarrow \mathbf{T}_o^g[\mathbf{n}_n(k, \cdot)]^T$
  - $\mathbf{n}_m(k, \cdot) \leftarrow \mathbf{n}_t(1:3)$
- end
- Transform vertex positions to  $\Leftrightarrow$  global frame using temporary vector ( $\mathbf{n}_t \in \mathbb{R}^{4 \times 1}$ )
- $\Leftrightarrow$  Output obstacle vertices ( $\mathbf{n}_m$ )

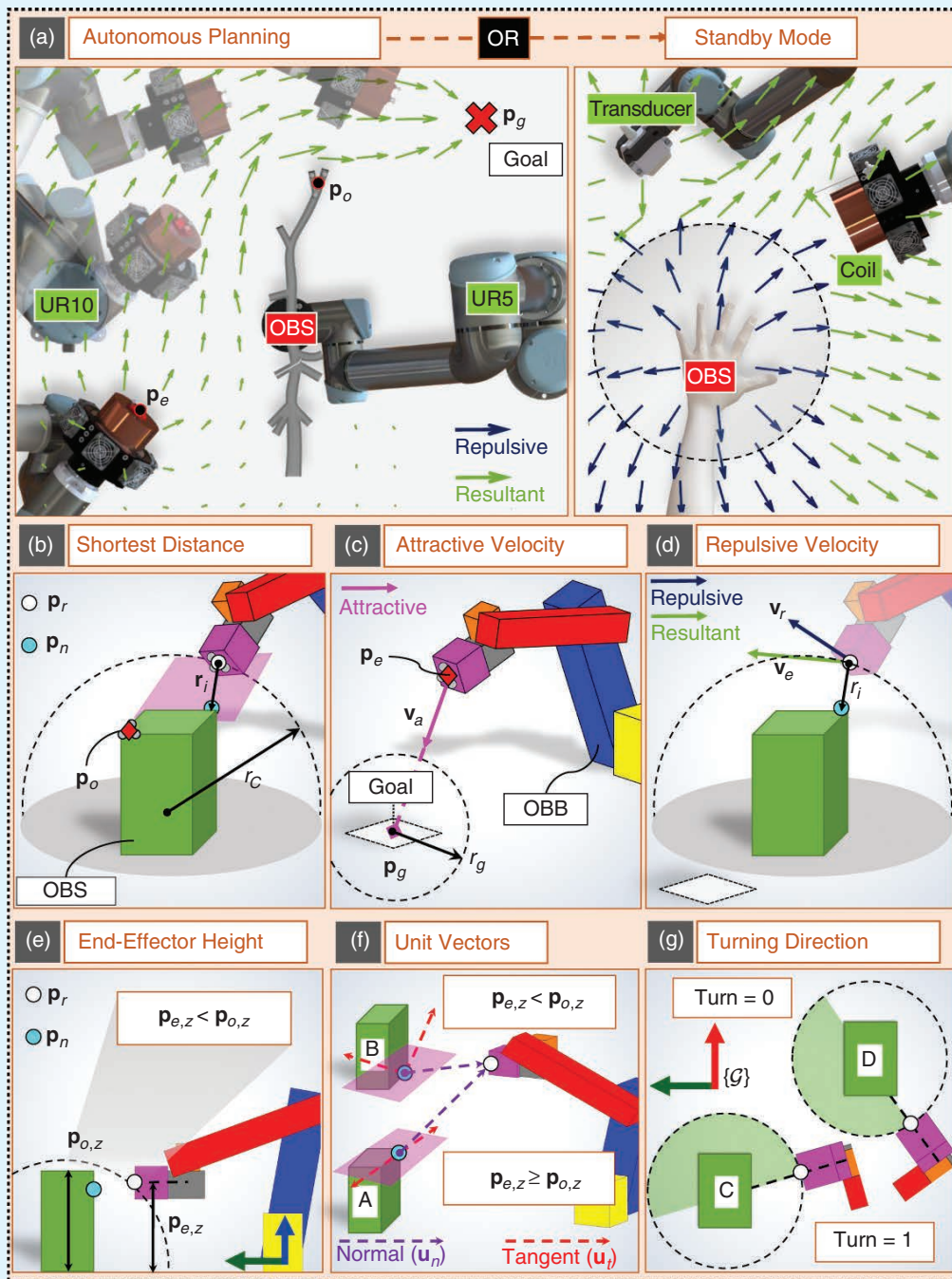


**Figure 5.** The GJK and VPF methods of intraoperative planning. (a) In this study, the collaborative control of the manipulators is aided by optical markers during two applications: the autonomous planning of a robot end effector and an interaction with a clinician during an endovascular intervention. In the latter, the hand is modeled as a dynamic OBS within a safety sphere. (b) Manipulators and OBSs are modeled as OBBs, each assigned to its own relative position ( $p_o$ ). The geometric vertices and edges of these boxes are used to derive the shortest vector ( $r_i$ ) pointing from the manipulator ( $p_r$ ) to the OBS ( $p_n$ ), which is enveloped in a safety hemisphere with radius ( $r_c$ ). (c) The velocity vector ( $v_a$ ) attracts the robot end-effector position ( $p_e$ ) so that it moves toward the goal position ( $p_g$ ) in a hemisphere with radius ( $r_g$ ). (d) The repulsive velocity ( $v_r$ ) exists when an OBS is in close proximity to the robot, and  $v_e$  is the resulting velocity vector of the end effector. (e) Once the manipulator enters the safety hemisphere, based on the end-effector height ( $p_{e,z}$ ) and OBS height ( $p_{o,z}$ ), perturbation velocities are generated. (f) The end effector can be moved sideways (OBS A) or upward (OBS B), depending on the direction of the tangent-unit vector ( $u_t$ ). (g) The tangent direction is represented by a Boolean variable ( $turn$ ) determined by calculating the end-effector position with respect to the OBS centroid in frame ( $\mathcal{G}$ ). The end effector turns right (OBS C) if it is to the right of the centroid or left (OBS D) otherwise.

second algorithm utilizes this tracking data to employ an online OBS-avoidance scheme (Algorithm 2a). Manipulators can be instructed to avoid points on obstacles, guide themselves to specific target poses, or execute a standby mode during an intervention [Figure 5(a)]. In all cases, trajectory parameters are defined in the form of safety sphere radii. These radii control the region where the end-effector velocity potential starts to decrease (in the case of attraction) or increase (in the case of repulsion). First, we define the critical radius ( $r_g \in \mathbb{R}^+$ ) around the end-effector target point ( $\mathbf{p}_g$ ). The second critical radius ( $r_c \in \mathbb{R}^+$ ) is around an obstacle. A near collision occurs when a manipulator's end effector (or any point on a link) approaches any point on the surface of an OBB within  $r_c$ . This is determined with the aid of a Gilbert-Johnson-Keerthi (GJK) algorithm [20]. The use of this algorithm is twofold. First, it calculates a pair of closest points between convex shapes, where one point ( $\mathbf{p}_r \in \mathbb{R}^3$ ) lies on the manipulator and the other lies ( $\mathbf{p}_n \in \mathbb{R}^3$ ) on the obstacle [Figure 5(b)]. Second, it is used to determine whether the end-effector TCP ( $\mathbf{p}_e$ ) is to the left or right of the OBB centroid with respect to the global reference frame. The latter enables us to implement a turning strategy, which is demonstrated in Algorithm 2b.

The end-effector velocities required for a manipulator TCP to reach a target are calculated using a modified, artificial velocity-potential field (VPF) method proposed in [21]. The potential function subjects the robot end-effector velocity vector ( $\mathbf{v}_e(\mathbf{p}_e) \in \mathbb{R}^3$ ) to an attractive force toward the goal [Figure 5(c)] and a repulsive force away from an OBS [Figure 5(d)]. The computed velocity potential field for an OBS is

$$\mathbf{v}_e(\mathbf{p}_e) = \mathbf{v}_a + \mathbf{v}_r, \quad (5a)$$

$$\mathbf{v}_a = -K_a \mathbf{u}_a (1 - e^{-\frac{\|\mathbf{p}_e - \mathbf{p}_g\|}{r_g}}), \quad (5b)$$

$$\mathbf{v}_r = -K_n \mathbf{u}_n (e^{-\frac{\|\mathbf{r}_i\|}{r_c}}) - K_t \mathbf{u}_t (e^{-\frac{\|\mathbf{r}_i\|}{r_c}}), \quad (5c)$$

depending on whether the potential creates an attractive ( $\mathbf{v}_a \in \mathbb{R}^3$ ) or repulsive ( $\mathbf{v}_r \in \mathbb{R}^3$ ) effect. In (5b),  $K_a \in \mathbb{R}$  is a positive gain for the attraction potential of the target point ( $\mathbf{p}_g \in \mathbb{R}^3$ ). In (5c),  $K_{n,t} \in \mathbb{R}$  are positive gains for the repulsion potentials for collision avoidance. Furthermore,  $\mathbf{r}_i = (\mathbf{p}_r - \mathbf{p}_n) \in \mathbb{R}^3$  is the shortest vector between the OBS and manipulator. The unit vectors are

### Algorithm 2a: OBS-avoidance algorithm

#### Inputs:

- $\mathbf{p}_e \in \mathbb{R}^3$   $\Leftrightarrow$  End-effector current position in  $\{\mathcal{G}\}$
- $\mathbf{p}_g \in \mathbb{R}^3$   $\Leftrightarrow$  End-effector target position in  $\{\mathcal{G}\}$
- $r_c, r_g \in \mathbb{R}^+$   $\Leftrightarrow$  Critical radii around OBS ( $r_c$ ) and target ( $r_g$ )
- $r_1, r_2 \in \mathbb{R}^+$   $\Leftrightarrow$  OBS-threshold margins
- $\mathbf{u}_b, \mathbf{l}_b \in \mathbb{R}^6$   $\Leftrightarrow$  Upper and lower manipulator joint velocity limits
- $\mathbf{n}_m \in \mathbb{R}^{8 \times 3}$   $\Leftrightarrow$  Real-time OBB coordinates

#### Outputs:

- $turn \in \mathbb{B}$   $\Leftrightarrow$  Boolean variable for turning direction
- $\mathbf{u}_n \in \mathbb{R}^3$   $\Leftrightarrow$  Unit vector for normal repulsive force
- $\dot{\mathbf{q}} \in \mathbb{R}^6$   $\Leftrightarrow$  Manipulator joint velocities

#### Initialization:

- 1 Obtain OBS vertices  $\mathbf{n}_m$   $\Leftrightarrow$  Call *Algorithm 1*
- Start manipulator trajectory to target position  $\Leftrightarrow$  While specified goal is not reached
- While  $\mathbf{p}_e \neq \mathbf{p}_g$  do  $\Leftrightarrow$  While specified goal is not reached
- 2  $(turn, \mathbf{r}_i) \leftarrow \mathbf{GJK}(\mathbf{p}_r, \mathbf{p}_n)$   $\Leftrightarrow$  Obtain turning variable and shortest vector from **GJK** [20]
- if  $\|\mathbf{norm}(\mathbf{r}_i)\| > r_c$   $\Leftrightarrow$  If critical radius is not exceeded
- 3  $\mathbf{v}_e \leftarrow \mathbf{v}_a$  (5b)  $\Leftrightarrow$  Calculate desired end-effector velocity
- 4  $\dot{\mathbf{q}} \leftarrow \mathbf{J}_g^{-1} \mathbf{v}_e$  (6)  $\Leftrightarrow$  Output joint velocities using pseudoinverse of  $\mathbf{J}_g$
- else if  $\|\mathbf{norm}(\mathbf{r}_i)\| \leq r_c$   $\Leftrightarrow$  If critical radius is exceeded
- 5  $\mathbf{u}_n \leftarrow \frac{\mathbf{r}_i}{\|\mathbf{r}_i\|}$   $\Leftrightarrow$  Unit vector for normal repulsive force
- 6  $\mathbf{u}_t \leftarrow \mathbf{Alg.2b}(turn, \mathbf{u}_n)$   $\Leftrightarrow$  Input turning operator and normal unit vector to *Algorithm 2b*
- 7  $\mathbf{v}_e \leftarrow \mathbf{v}_a + \mathbf{v}_r$  (5)  $\Leftrightarrow$  Calculate desired end-effector velocity
- 8  $\mathbf{J}_{c,v} \leftarrow$  (8)  $\Leftrightarrow$  Update contact-point Jacobian
- 9  $s(\mathbf{r}_i) \leftarrow \begin{cases} 1, & \mathbf{r}_i \geq r_2 \\ \sin^2\left(\frac{\pi}{2} \frac{\mathbf{r}_i - r_1}{r_2 - r_1}\right), & r_1 < \mathbf{r}_i < r_2 \\ 0, & \mathbf{r}_i \leq r_1 \end{cases}$   $\Leftrightarrow$  Derive smoothing function between OBS threshold margins ( $r_1, r_2$ )
- 10  $\mathbf{A} \leftarrow \begin{bmatrix} \text{sgn}(\mathbf{p}_{n,x} - \mathbf{p}_{r,x}) \mathbf{J}_{c,v}(1, \cdot) \\ \text{sgn}(\mathbf{p}_{n,y} - \mathbf{p}_{r,y}) \mathbf{J}_{c,v}(2, \cdot) \\ \text{sgn}(\mathbf{p}_{n,z} - \mathbf{p}_{r,z}) \mathbf{J}_{c,v}(3, \cdot) \end{bmatrix}$   $\Leftrightarrow$  Calculate critical point Jacobian matrix (**A**)
- 11  $\mathbf{b} \leftarrow s(\mathbf{r}_i) \begin{bmatrix} \max(\mathbf{A}(1, \cdot); \dot{\mathbf{q}}_{r2}, 0) \\ \max(\mathbf{A}(2, \cdot); \dot{\mathbf{q}}_{r2}, 0) \\ \max(\mathbf{A}(3, \cdot); \dot{\mathbf{q}}_{r2}, 0) \end{bmatrix}$   $\Leftrightarrow$  Calculate coefficient vector from joint velocities ( $\dot{\mathbf{q}}_{r2}$ ) at link-OBS distance ( $\|\mathbf{norm}(\mathbf{r}_i)\| = r_2$ )
- 12  $\mathbf{A}\dot{\mathbf{q}} \leq \mathbf{b}$   $\Leftrightarrow$  Generate inequality constraints
- 13  $\dot{\mathbf{q}} \leftarrow f(\dot{\mathbf{q}})$  (10)  $\Leftrightarrow$  Optimize joint velocities using QP solver
- end  $\Leftrightarrow$  Prescribe joint velocities
- end

defined as  $\mathbf{u}_a = \mathbf{p}_e - \mathbf{p}_g / \|\mathbf{p}_e - \mathbf{p}_g\|$ ,  $\mathbf{u}_n = \mathbf{r}_i / \|\mathbf{r}_i\|$ , and  $\mathbf{u}_t = \mathbf{r}_i^\perp / \|\mathbf{r}_i^\perp\| \in \mathbb{R}^3$ . When the end effector is outside the region spanned by the critical radius ( $r_c$ ), it moves directly toward the goal, subject to  $\mathbf{v}_a$ . The original VPF method is modified by adding a small perturbation velocity to the repulsive forces once a threshold distance between the OBS and end-effector position is reached. By implementing a turning strategy in the direction perpendicular ( $\perp$ ) to  $\mathbf{u}_n$  and away from the OBS surface, the perturbation enables the end effector to move toward the target goal. This vector is influenced by the end effector's  $z$  position ( $\mathbf{p}_{e,z}$ ) and the height of the OBS ( $\mathbf{p}_{o,z}$ ) in ( $\{\mathcal{G}\}$ ). Details of the exact direction are outlined in Algorithm 2b and illustrated in Figure 5(e)–(g).



### Algorithm 2b: Turning strategy for manipulator end effector

#### Inputs:

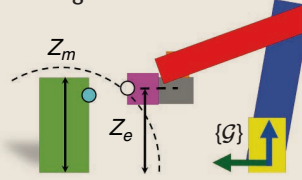
- $\mathbf{n}_m \in \mathbb{R}^{8 \times 3}$   $\Leftrightarrow$  Real-time OBB coordinates  
 $\mathbf{p}_e \in \mathbb{R}^3$   $\Leftrightarrow$  End-effector current position in  $\{\mathcal{G}\}$   
 $r_c \in \mathbb{R}^+$   $\Leftrightarrow$  Critical radius around OBS  
 $turn \in \mathbb{B}$   $\Leftrightarrow$  Boolean variable for turning direction  
 $\mathbf{u}_n \in \mathbb{R}^3$   $\Leftrightarrow$  Unit vector for normal repulsive force

#### Outputs:

- $z_e \in \mathbb{R}$   $\Leftrightarrow$  End-effector  $z$  position  
 $z_m \in \mathbb{R}$   $\Leftrightarrow$  Maximum OBS  $z$  position  
 $\mathbf{u}_t \in \mathbb{R}^3$   $\Leftrightarrow$  Unit vector for tangent repulsive force

#### Initialization:

- 1  $z_e \leftarrow \mathbf{p}_e(3)$   $\Leftrightarrow$  Obtain end-effector height
- 2  $z_m \leftarrow \mathbf{n}_m(1,3)$   $\Leftrightarrow$  Obtain maximum OBS height
- if  $z_e \geq z_m$   $\Leftrightarrow$  If end effector is above OBS
  - if  $turn = 0$   $\Leftrightarrow$  If end effector should turn left
    - 3  $\mathbf{u}_t \leftarrow [\mathbf{u}_n(2) \quad -\mathbf{u}_n(1) \quad 0]$
  - else  $\Leftrightarrow$  End effector should turn right
    - 4  $\mathbf{u}_t \leftarrow [-\mathbf{u}_n(2) \quad \mathbf{u}_n(1) \quad 0]$
- else if  $z_e < z_m$   $\Leftrightarrow$  If end effector is below OBS maximum height
  - if  $turn = 0$ 
    - 5  $\mathbf{u}_t \leftarrow [\mathbf{u}_n(2) \quad -\mathbf{u}_n(1) \quad 1]$
  - else
    - 6  $\mathbf{u}_t \leftarrow [-\mathbf{u}_n(2) \quad \mathbf{u}_n(1) \quad 1]$



### Strategy for Closed-Loop Trajectory Control

The global planning of trajectories is generally performed in a scenario where no OBSs are present. In this case, using the task velocity in (5a), joint velocities can be computed from the geometric-manipulator Jacobian-inverse ( $\mathbf{J}_g \in \mathbb{R}^{6 \times n}$ ) approach satisfying

$$\mathbf{v}_e(\mathbf{p}_e) = \mathbf{J}_g \dot{\mathbf{q}}, \quad (6)$$

where  $\mathbf{q} = \{q_1, q_2, \dots, q_n\} \in \mathbb{R}^n$  denotes the set of joint angles for  $n$  joints. However, the planning algorithm is designed so that the robot must avoid obstacles within its vicinity, including collisions with its links. In this case, we define a contact-point Jacobian ( $\mathbf{J}_c \in \mathbb{R}^{6 \times i}$ ), where  $i$  represents the number of manipulator links, as outlined in [18] and [22]. Generally, for an arbitrary point ( $\mathbf{p}_r$ ) on any link ( $j \in 1, \dots, i$ ), the Jacobian is defined as

$$\mathbf{J}_c = \begin{bmatrix} \mathbf{J}_{c,v} \\ \mathbf{J}_{c,\omega} \end{bmatrix}, \quad (7)$$

where the linear velocity component is defined as

$$\mathbf{J}_{c,v} = \begin{cases} z_{i-1}^0 \times (\mathbf{p}_r - o_{i-1}^0), & \forall i \leq j \\ \mathbf{0}, & \forall i > j, \end{cases} \quad (8)$$

and the angular velocity component is defined as

$$\mathbf{J}_{c,\omega} = \begin{cases} z_{i-1}^0, & \forall i \leq j \\ \mathbf{0}, & \forall i > j, \end{cases} \quad (9)$$

where  $z_{i-1}^0 = \mathbf{R}_{i-1}^0 \mathbf{k}$  represents the transformation from the manipulator's base frame to link  $i$ , with  $\mathbf{k} = [0, 0, 1]^T$ , and  $o_{i-1}^0$  represents the translation from the previous link's base frame.

In our strategy, outlined in Algorithm 2a, once  $\|\mathbf{r}_i\|$  is smaller than a critical radius, only the velocity of the point on the link ( $j$ ) closest to the OBS is considered. We then employ only  $\mathbf{J}_{c,v}$ , which results in a redundant task that is resolved through a quadratic programming (QP) algorithm outlined in [23]. This algorithm solves the inverse kinematics problem, which is implemented using the CPLEX application programming interface (ILOG Studio V12.6.1, IBM, New York):

$$\begin{aligned} \min f(\dot{\mathbf{q}}) &= \frac{1}{2} \dot{\mathbf{q}}^T \mathbf{Q} \dot{\mathbf{q}} \\ \text{subject to } &\mathbf{A} \dot{\mathbf{q}} \leq \mathbf{b} \\ &\text{and } \mathbf{l}_b \leq \dot{\mathbf{q}} \leq \mathbf{u}_b. \end{aligned} \quad (10)$$

Joint velocities ( $\dot{\mathbf{q}}$ ) are minimized subject to the dynamic inequality constraint ( $\mathbf{A} \dot{\mathbf{q}} \leq \mathbf{b}$ ), which is the collision-free criterion, while, simultaneously, joint velocity constraints ( $\mathbf{l}_b \leq \dot{\mathbf{q}}, \mathbf{l}_b \in \mathbb{R}^6$  and  $\mathbf{u}_b \geq \dot{\mathbf{q}}, \mathbf{u}_b \in \mathbb{R}^6$ ) are satisfied. These joint velocities are chosen as  $[-1.05, 1.05]$  rad/s for joints (1–3) and  $[-1.57, 1.57]$  rad/s for joints (4–6). Furthermore,  $\mathbf{A} \in \mathbb{R}^{3 \times 6}$  is the critical-point Jacobian matrix, and  $\mathbf{b} \in \mathbb{R}^3$  is the velocity prescribed to

push the manipulator link ( $j$ ) away from the obstacle. To avoid sudden joint deceleration, a smoothing function  $[s(\mathbf{r}_i)]$  is used to gradually decrease  $\mathbf{A} \dot{\mathbf{q}}$  within a margin of space. In Algorithm 2a (line 9), the thresholds of these inner and outer margins are chosen as  $r_1 = 30$  mm and  $r_2 = 50$  mm. The inequality is imposed only when the minimum distance ( $\|\mathbf{r}_i\|$ ) is less than the outer safety threshold ( $r_2$ ). Next,  $\mathbf{Q}$  is the coefficient matrix, arbitrarily chosen as an identity matrix ( $\mathbf{Q} = \mathbf{I}_{6 \times 6}$ ) to assign equal weights to all joint velocities. Finally, we input the obtained set of joint velocities to the embedded joint velocity controller of the manipulator.

### Experiments

In this section, we evaluate the ARMM system's tracking scheme, as presented in the "Robot Navigation During Endovascular Interventions" section. This evaluation is used as a benchmark for the quality assessment of the performed experiments. The experimental plan is described, followed by a summary and the results of each experiment. Based on the aspects of our planner, displayed in Figure 5(a), we implement two experiments using the ARMM system. Table 1 lists the subsystems employed in each experiment.

### Experiment Plan

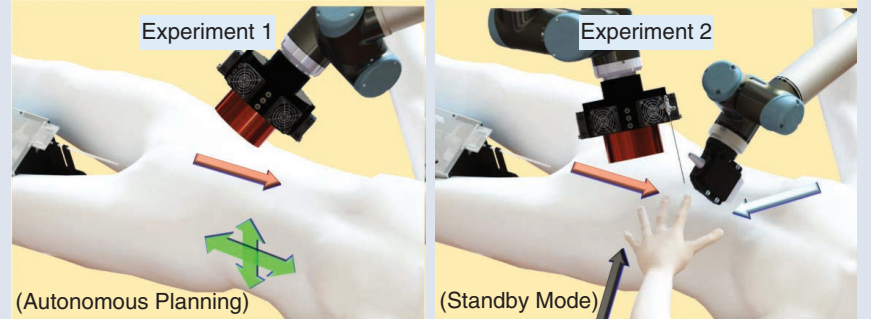
Utilizing the control strategy of the ARMM system (Figure 6), different experimental cases can be demonstrated. In this study, we detail an autonomous planning strategy that does not include a clinician as well as an intraoperative decision

support where both manipulators assist a clinician. The results for experiments 1 and 2 are shown in Figure 7.

The first experiment [Figure 7(a)] is related to arterial reperfusion, where we guide a magnetic endovascular catheter (ClariVein infusion catheter, Merit Medical, South Jordan, Utah) through mockup arterial branches with simulated breathing motions. First, a CAD model of the systemic arterial tree is designed and 3D-printed as a mockup structure. Seven principle abdominal aorta branches are modeled based on a different takeoff angle with respect to the main arterial branch [Figure 7(b)]. In our actuation strategy, we deflect the catheter tip to the desired angle ( $\alpha$ ) by controlling the magnetic wrenches using  $\mathbf{W}_\mu$  (2). For this to occur, the UR10 has to traverse to seven poses while avoiding a collision with the moving artery. To determine the UR10's series of end-effector poses (i.e., the poses of the electromagnet), we develop a feed-forward controller. We induce the rotation of

the catheter segment ( $\rho_L$ ) on a 2D plane [Figure 4(d)] by prescribing a positive or negative current in the EM coil. This current is controlled using an XEL-230-40 amplifier

**Table 1. The ARMM system experiments.**



Experiment	ARMM System Apparatus				
	Tracker	CID	Electromagnet	US	Dynamic OBSs
1: Trajectory planning and collision avoidance	X	X	X	—	X
2: Interaction with a user during an intervention	X	X	—	X	X

The illustrations show the two experimental cases with a virtual patient, including the CID, the EM coil attached to the UR10 and the US transducer attached to the UR5.

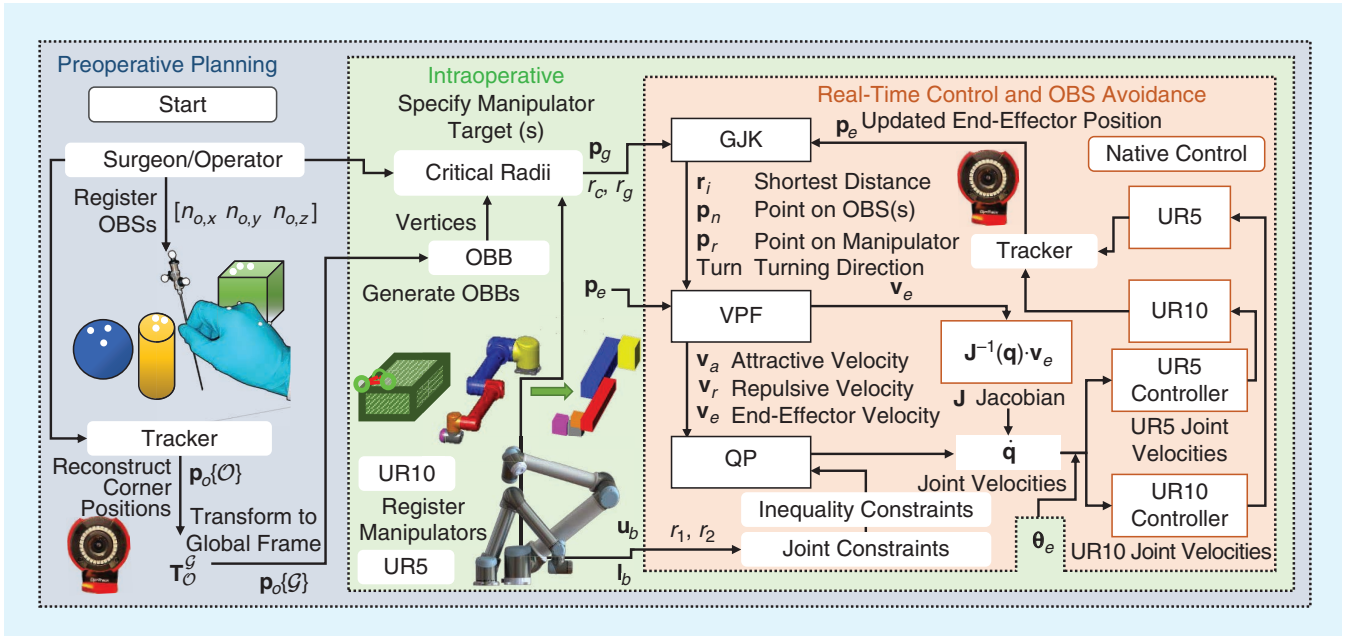


**Figure 6.** A block diagram of the OBS-avoidance algorithm for the two serial-link manipulators (UR10/UR5). The high-level control layer (preoperative planning) acquires the catheter targets supplied by the user (clinician) and the reconstructed data from the vision-based 3D tracking system. Following this, a GJK algorithm computes the minimum distance ( $r_i$ ) between a point on the manipulator ( $\mathbf{p}_r$ ) and on an OBS ( $\mathbf{p}_n$ ) in the workspace while adhering to safety margins and critical radii ( $r_c$  and  $r_g$ ). These algorithms are implemented after visualizing the system workspace's 3D environment and enveloping objects by OBBs. The VPF method requires the position of an OBS with dimensions ( $n_{o,x} \times n_{o,y} \times n_{o,z}$ ) provided by markers and the end-effector position ( $\mathbf{p}_e$ ). The  $\mathbf{v}_a$  is the velocity effect that attracts the robot to move toward the goal ( $\mathbf{p}_g$ ),  $\mathbf{v}_r$  is the repulsive velocity effect to avoid a collision between the robot and OBS, and  $\mathbf{v}_e$  is the end effector's resulting velocity vector. The VPF calculates the superposition of the attractive (end-effector goal position) and repulsive (OBSs) potential functions. This results in joint velocity ( $\mathbf{q}$ ) commands, which are minimized through an online QP algorithm. The inputs to the QP algorithm are the upper ( $\mathbf{u}_b$ ) and lower ( $\mathbf{l}_b$ ) joint velocity constraints; the margins ( $r_1$  and  $r_2$ ) and coefficients are provided in Algorithm 2a.

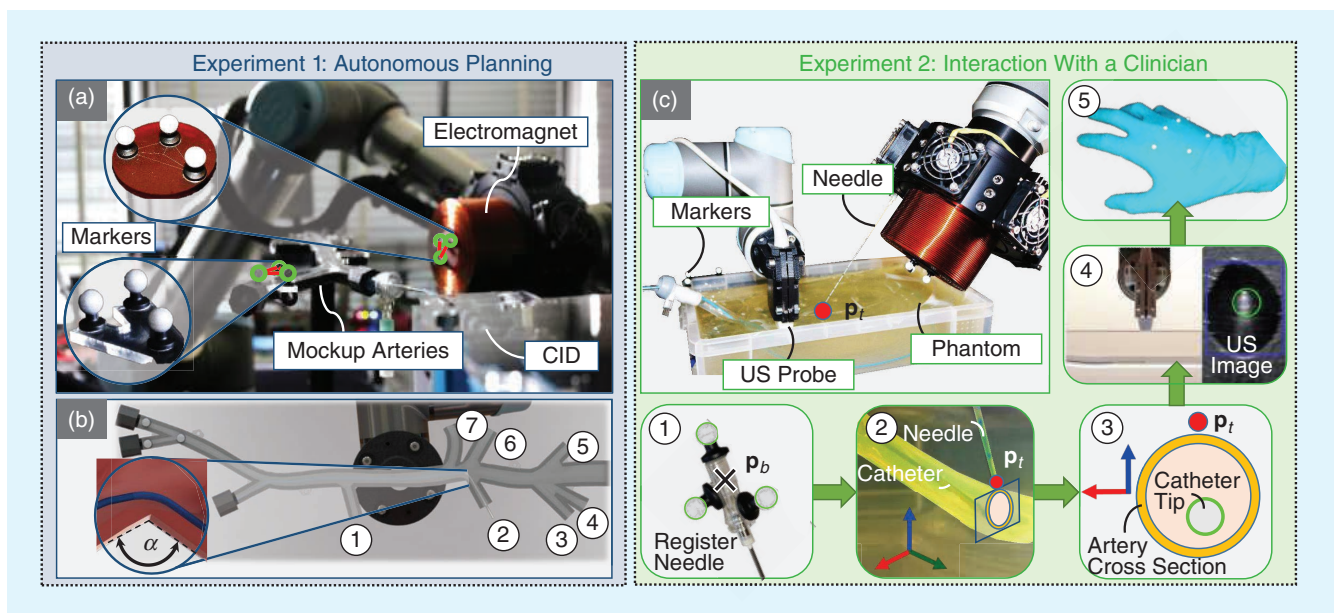


**Figure 7.** The experimental setups. (a) Experiment 1 demonstrates the real-time OBS-avoidance strategy without a clinician. The mockup arterial structure is placed on the end effector of the UR5. The CID and UR10 end effector are also registered. (b) During the experiment, the CID inserts the catheter, followed by the autonomous magnetic actuation of the catheter tip. The aim is to magnetically deflect the catheter tip in seven known angles ( $\alpha$ : (1) – (7)) inside the mockup arteries. (c) Experiment 2 shows an endovascular intervention with a clinician. A needle is used to provide targets, which, in turn, define the poses for both manipulators. ① The needle is registered within the workspace utilizing markers on its base position ( $p_b$ ). ② A view inside the phantom shows the needle tip as well as the catheter inside the tube. ③ The needle-tip position ( $p_t$ ) and planar orientation are calculated to determine the pose of the UR5. ④ The UR5 reaches its pose to place the US transducer on the phantom surface. The catheter is then inserted using the CID to reach the target. 2D template-matching of the catheter tip ensures that the desired target has been reached. ⑤ During the entire intervention, when the clinician’s hand enters the workspace, the OBS-avoidance strategy executes a standby state.

(Copley Controls, Boston) connected via EtherCAT, as calculated using (3).

The second experiment [Figure 7(c)] relates to a more realistic medical scenario. We demonstrate a presurgical localization methodology for target registration inside a gelatinous phantom. During this experiment, we insert the same catheter into a gelatinous phantom fitted with a silicon tube and aim to demonstrate how the robots work together; the intervention can be interrupted by the clinician’s hand. A needle is attached to the UR10 and tracked while it is inserted into the phantom. The UR5 then places the US transducer above the target, which commences the insertion of the catheter.

### Experiment 1: Magnetic Actuation

The mockup structure is registered preoperatively using markers [Figure 7(a)] and placed on the end effector of the UR5. This is followed by a preliminary calibration experiment to determine the coil current and catheter-insertion length. One trajectory (trajectory 1) of the UR10 is executed using the OBS-avoidance algorithm. This trajectory consists of a combination of seven subtrajectories, each traversing the UR10 end effector to a pose that terminates opposite an arterial branch. The magnetic torque applied to the tip of the catheter is determined empirically after each end-effector pose has been reached.

Next, we evaluate the OBS-avoidance algorithm using empirical results from the first experiment. We implement the

same trajectory while displacing the mockup structure, first horizontally (trajectory 2) and then vertically (trajectory 3), as shown in Figure 8. We impose a sinusoidal motion with an amplitude of 5 mm to simulate the respiratory cycle of a breathing patient. We then insert the catheter again, with the insertion length obtained from the results of trajectory 1. The poses of the UR10 and the current supply to the coil are defined as inputs. Three trials are conducted for each trajectory.

The results of experiment 1 are presented in Figure 8. We report the accuracies of the tracking system (3D reconstruction error) and the trajectory planner (QP planner versus actual trajectory) in Table 2. The resulting input currents range from 1 to 6 A, with magnetic fields generated between 20 and 80 mT, which is sufficient to deflect the magnetic catheter at a safe distance from the target artery. With this distance, it is assumed that the electromagnet can be maneuvered without colliding with or touching the patient. This is visualized by a safety hemisphere around the obstacle (Figure 8). The reconstruction of the objects is performed with a mean error of 2.9 mm. Furthermore, the UR10 autonomously positions the EM coil without any collisions at an accuracy of 1.55 mm (RMSE).

### Experiment 2: Collaborative Control

In this experiment, the collaborative control of two surgical robots is evaluated. We implement the obstacle-avoidance algorithm in the setup shown in Figure 7(c). The aim is to demonstrate a dynamic collision-avoidance scenario

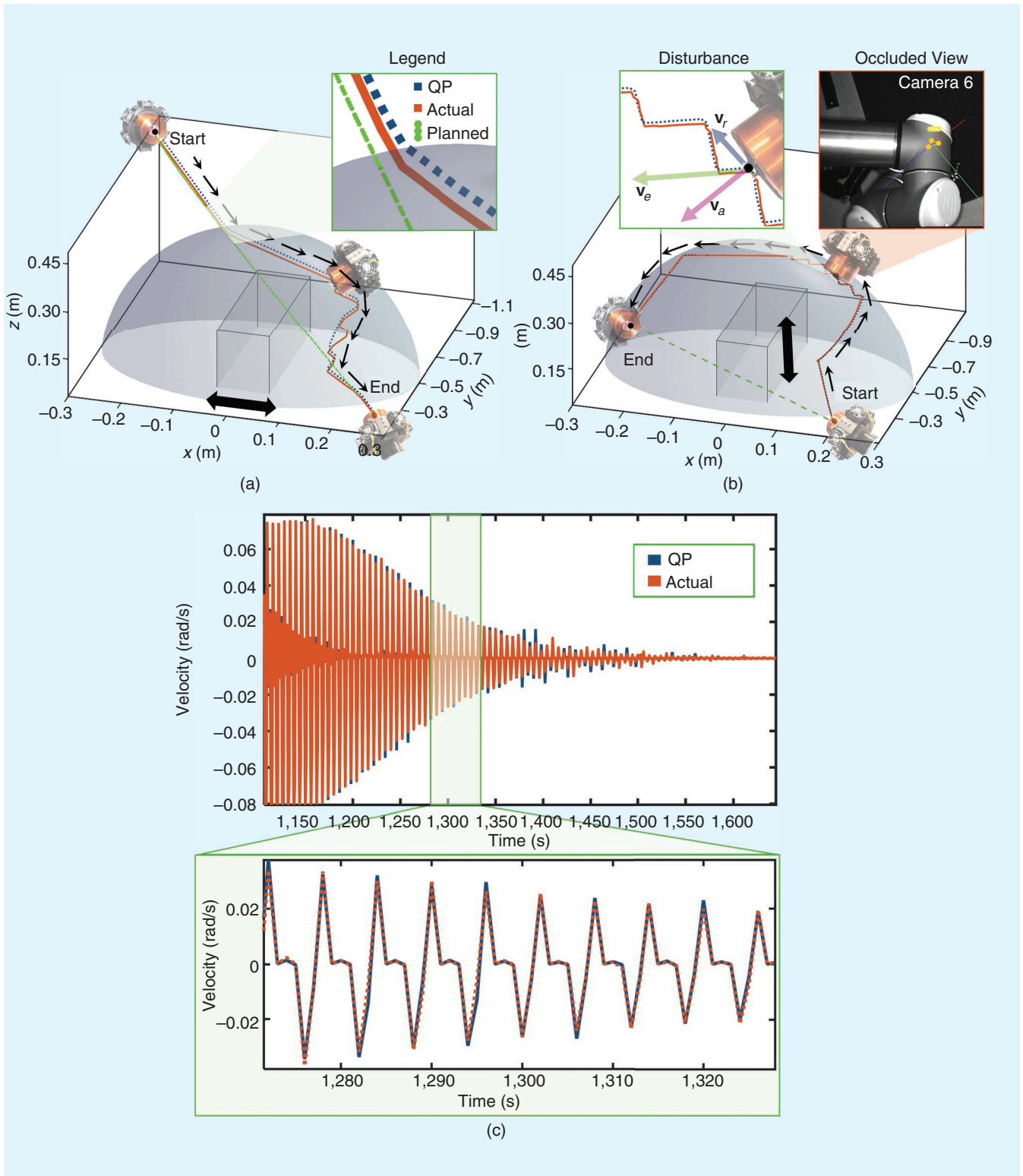


**Figure 8.** The results of experiment 1. This experiment concerns the online trajectory and OBS/collision avoidance of a robotic end effector during the magnetic deflection of an endovascular catheter in seven targets. (a) The move from the initial configuration to target 1 during trajectory 2. The end effector (orange) avoids a mockup arterial structure that is displaced horizontally. This trajectory is shown in the 3D capture volume around the BB of the arterial structure, which is enveloped in a safety hemisphere. The end effector first follows a planned trajectory obtained from (7), indicated in green, after which the QP algorithm calculates the joint velocities to obtain the desired end-effector position (blue). (b) The move from target 5 to 6. The end effector avoids the arterial structure during vertical motions. The left-side inset shows the reactive planner that results from these motions due to the attractive-velocity vector ( $v_a$ ), repulsive velocity ( $v_r$ ), and velocity vector of the end effector ( $v_e$ ). The right-side inset from camera 6 illustrates the consistent tracking of the end effector despite an occlusion. (c) The joint velocity profile of joint 2 indicates the calculated (blue) versus the actual (orange) velocities.

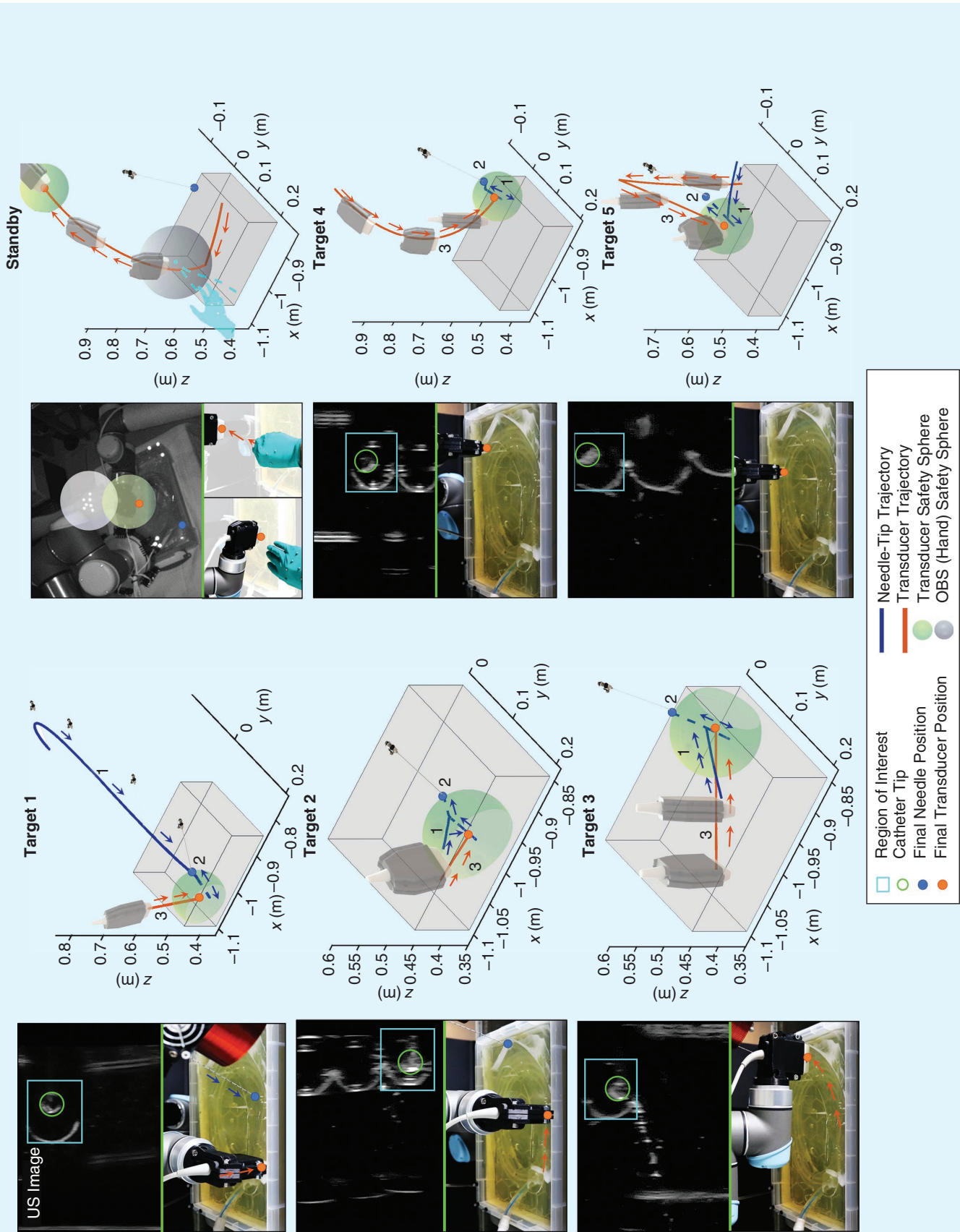


**Figure 9.** The results of the second experiment. Five catheter-tip targets are prescribed in a gelatin phantom using a surgical needle. The US transducer is enveloped by a green safety sphere, which the second robot must avoid. The transducer is guided across the phantom surface to reach the targets. Refer to the accompanying video, which can be found as supplemental material for this article in *IEEE Xplore*, that illustrates these trajectories.

involving multiple robots and another obstacle (a moving hand), as shown in Table 1. A catheter is inserted in a gelatinous phantom fitted with a silicon tube.

The procedure is as follows. First, a safety sphere is generated around the transducer and the clinician's hand, as pictured in Figure 7(c), inset ⑤. We then designate a target in the phantom using a surgical needle that is attached to the UR10. The needle base position is tracked, enabling us to derive the tip position in 3D. Once this position is known, the planar orientation of the US transducer and its TCP target point ( $\mathbf{p}_g$ ) are derived geometrically. The transducer should be rotated to provide a true axial cross section of the artery that is perpendicular to the path of the artery's centerline. The unit vector of (2) should coincide with the transducer's  $x$ -axis ( $\hat{X}_t$ ) [Figure 4(e)], which is the axis of rotation for adjusting the transducer's yaw angle. During this trajectory, the UR10 should avoid the safety sphere that represents the US probe (Figure 9).

After inserting the needle, the UR10 moves to a pose outside the region enveloped by the sphere. Once the transducer is safely positioned, the catheter is inserted using the CID. We then detect the catheter tip in the US images within the specified plane by employing image-template matching. We utilize the normal component of  $\mathbf{v}_r$  in (5c) to instruct the robots to enter an emergency standby mode, ensuring that the end effectors avoid the clinician's hand, which is enveloped by another safety sphere. The US frames of the targets in experiment 2 are shown in Figure 9, where a green circle represents the catheter tip inside the silicon tube (blue square). Collaborative control (i.e., intraoperative interaction with both robotic arms) is successfully implemented.

## Discussion

The results of these experiments (Table 2, Figures 8 and 9) indicate an accurate real-time OBS-avoidance strategy that can be beneficial during a surgical intervention where high accuracy is required when placing needles, holding imaging transducers, and maneuvering surgical tools using robotic arms. The proposed tracking scheme can aid autonomous cooperative interaction with multiple surgical robots, especially when a patient moves during surgery or the clinician has to intervene.

The VPF method successfully takes into account the dynamics of both robots and moving obstacles. The robots adapt quickly to disturbances in the ARMM environment; the joint velocities take a maximum of 6 ms to be calculated. We notice a higher maximum error for static obstacles (trajectory 1). This may be due to the higher velocities during the static experiment in comparison with the dynamic one, which negatively affects the cameras' tracking capabilities. However, in all experiments, collision was avoided between the two robots and surrounding (still or moving) obstacles.

Our methods combine the strengths of tracker-based motion planning and native robot control to prescribe trajectories that enable surgical robots to 1) autonomously avoid static and dynamic OBSs and 2) simultaneously reach a target goal specified by an end-user. The use of optical tracking

**Table 2. The 3D-reconstruction errors.**

3D-Reconstruction Error (Triangulation)					
Trajectory		$\epsilon_m$ (mm)	$\epsilon_\sigma$ (mm)	$\epsilon_{RMS}$ (mm)	
Experiment 1	1	3.79	2.92	2.99	
	2	2.15	1.65	1.82	
	3	2.58	1.98	2.07	
Trajectory-planner error (QP versus actual)					
Experiment 1	1	2.49	1.25	1.55	
	2	2.56	1.06	1.45	
	3	2.42	1.85	1.9	
Overall results (experiments 1 and 2)					
Optimization routine (rad/s)			1.24	1.57	
Tracking (mm)		Static environment (mean error)			$0.5 \pm 0.3$
		Dynamic environment (mean error)			$2.3 \pm 0.6$

Errors indicate the accuracy with which objects are triangulated inside the ARMM system workspace. The ground truth for reconstruction is the end-effector position estimated using the low-level controller of each manipulator (UR10/UR5). The 3D-reconstruction error (triangulation) results represent the maximum ( $\epsilon_m$ ), mean ( $\epsilon_\sigma$ ), and RMS ( $\epsilon_{RMS}$ ) errors (in millimeters) between the position as estimated from angular data provided by the robot's encoders and the position as tracked by the eight cameras. Trajectory-planner errors resulting from the OBS-avoidance algorithm are indicated in radians per second for the optimization routine, followed by the overall tracking errors of both experiments.

to EMT as a primary localizer offers several benefits, including an increased range and effective use within a magnetic-actuation system. However, one of the limitations introduced in this study relates to conducting experiments in a realistic, clinically relevant scenario. In reality, the amplitude and period of breathing motions vary with time and among patients. Furthermore, preoperative patient-vasculature data would be more relevant when investigating accurate 3D catheter-tip positioning in vivo. Since the focus of the experiments was on the task-space control of the robotic end effectors, we have not investigated the accurate magnetic control of a catheter tip based on real-time subsurface imaging. However, this leaves room for future studies conducted with the ARMM system.

A second limitation of optical tracking is that it is only useful for monitoring surgical instruments outside the body. Moreover, tracking the instruments requires a direct line of sight with at least two cameras. To solve this, sensor-based fusion techniques can be investigated that combine optical tracking and US imaging to record flexible objects inside the body. Rigid bodies can be constructed from active markers instead of the passive reflective markers used in this study. Such markers emit radio frequency signals and can be integrated with accelerometer-gyroscope sensors. This would enable the sensing of moving objects' angular velocities, which can be useful for providing additional coordinate data

in case of occlusions. A potential drawback could be related to the flexibility and size of our system: a fixed tracking system is an important requirement; hence, optimally positioning the cameras may be time consuming. Recalibration of the tracking system can also be challenging since it consists of eight cameras as opposed to single stereo-camera trackers, such as the NDI Polaris. Fortunately, the Motive software can adjust the system calibration to account for changes, even drastic ones, in the positions and orientations of the cameras.

Improving the mobility of the ARMM operating table may be challenging due to its size (Figure 2). However, in practice, the entire system can be transported between operating rooms since each of the subsystems is mobile. Such a scenario only implies that an additional calibration step would be necessary, as explained in the “Preoperative Planning: Workspace Registration” section. Finally, the magnetic field generated by the EM coil may affect the serial-link manipulator’s encoders. Since the encoders used in the joints of the UR10 are magnetic, they can be damaged when high external magnetic fields are present. We took this into account when we designed the electromagnet and calculated its offset from the end-effector surface. The electromagnet has been tested at a maximum of 15 A, indicating no malfunction. As a safety measure, in this study’s experiments, we did not exceed  $\pm 6$  A.

### Conclusions and Future Work

We presented a tracking and navigation technique that aims to bring the ARMM system a step closer to clinical studies. By incorporating two surgical robots, the system reduces the constraints of similar actuation systems, including an insufficient workspace, limited DoFs for surgical tools, and bulky components. Furthermore, we introduced an obstacle-avoidance strategy based on marker-aided optical tracking. We demonstrated the 3D reconstruction accuracy of the tracking system and the velocity errors of the optimization routine. The navigation to target robot poses was accomplished around static and dynamic obstacles with an overall 3D tracking accuracy of  $0.5 \pm 0.3$  mm (static) and  $2.3 \pm 0.6$  mm (dynamic). For the proposed optimization routine, an error of 1.57 rad/s (RMSE) and a mean error of 1.24 rad/s were achieved.

We plan to demonstrate the clinical feasibility of the ARMM system by remotely steering a magnetically actuated catheter inside a realistic US phantom. Such a phantom should represent real arteries, including simulated blood flow and breathing motions. Improved magnetic-catheter designs can be tested using the ARMM system, and the availability of more than two manipulators may enable additional control capabilities for this magnetic system, including the possibility of compensating for organ motion in multiple targets. We envision our system for an operating room that can readily integrate the latest US imaging and interventional technologies.

### Acknowledgments

This article is dedicated to the memory of Guilherme Phillips Furtado, who passed away during its preparation. This work was supported by funds from the Netherlands Organization for Scientific Research (Innovational Research Incentives Scheme Vidi: SAMURAI project no. 14855).

### References

- [1] A. R. Lanfranco, A. E. Castellanos, J. P. Desai, and W. C. Meyers, “Robotic surgery: A current perspective,” *Ann. Surg.*, vol. 239, no. 1, pp. 14–21, 2004. doi: 10.1097/01.sla.0000103020.19595.7d.
- [2] K. D. Chang, A. A. Raheem, and K. H. Rha, “Novel robotic systems and future directions,” *India J. Urol.*, vol. 34, no. 2, pp. 110–114, 2018. doi: 10.4103/iju.IJU\_316\_17.
- [3] S. B. Choi and S. Y. Choi, “Current status and future perspective of laparoscopic surgery in hepatobiliary disease,” *Kaohsiung J. Med. Sci.*, vol. 32, no. 6, pp. 281–291, 2016. doi: 10.1016/j.kjms.2016.05.006.
- [4] N. Simaan, R. M. Yasin, and L. Wang, “Medical technologies and challenges of robot-assisted minimally invasive intervention and diagnostics,” *Annu. Rev. Control, Robot., Auton. Syst.*, vol. 1, pp. 465–490, May 2018. doi: 10.1146/annurev-control-060117-104956.
- [5] C. M. Heunis, J. Sikorski, and S. Misra, “Flexible instruments for endovascular interventions: Improved magnetic steering, actuation, and image-guided surgical instruments,” *IEEE Robot. Autom. Mag.*, vol. 25, no. 3, pp. 71–82, 2018. doi: 10.1109/MRA.2017.2787784.
- [6] J. Sikorski, C. M. Heunis, F. Franco, and S. Misra, “The ARMM system: An optimized mobile electromagnetic coil for non-linear actuation of flexible surgical instruments,” *IEEE Trans. Magn.*, vol. 55, no. 9, pp. 1–9, 2019. doi: 10.1109/TMAG.2019.2917370.
- [7] N. Enayati, E. De Momi, and G. Ferrigno, “Haptics in robot-assisted surgery: Challenges and benefits,” *IEEE Rev. Biomed. Eng.*, vol. 9, pp. 49–65, Mar. 2016. doi: 10.1109/RBME.2016.2538080.
- [8] D. M. Kwartowitz, M. I. Miga, S. D. Herrell, and R. L. Galloway, “Towards image guided robotic surgery: Multi-arm tracking through hybrid localization,” *Int. J. Comput. Assist. Radiol. Surg.*, vol. 4, no. 3, pp. 281–286, 2009. doi: 10.1007/s11548-009-0294-1.
- [9] Q. C. Nguyen, Y. Kim, and H. Kwon, “Optimization of layout and path planning of surgical robotic system,” *Int. J. Control, Autom. Syst.*, vol. 15, no. 1, pp. 375–384, 2017. doi: 10.1007/s12555-015-0418-z.
- [10] H. Kenngott et al., “Development of a navigation system for minimally invasive esophagectomy,” *Surg. Endosc.*, vol. 22, no. 8, pp. 1858–1865, 2008. doi: 10.1007/s00464-007-9723-9.
- [11] H. Ren and H. Banerjee, “A preface in electromagnetic robotic actuation and sensing in medicine,” in *Electromagnetic Actuation and Sensing in Medical Robotics*, H. Ren and J. Sun, Eds. New York: Springer-Verlag, 2018, pp. 1–10.
- [12] H. Kenngott et al., “Magnetic tracking in the operation room using the da Vinci® telemanipulator is feasible,” *J. Robot. Surg.*, vol. 7, no. 1, pp. 59–64, 2013. doi: 10.1007/s11701-012-0347-2.
- [13] D. D. Frantz, A. Wiles, S. Leis, and S. Kirsch, “Accuracy assessment protocols for electromagnetic tracking systems,” *Phys. Med. Biol.*, vol. 48, no. 14, pp. 2241–2251, 2003. doi: 10.1088/0031-9155/48/14/314.
- [14] R. Nuzzi and L. Brusasco, “State of the art of robotic surgery related to vision: Brain and eye applications of newly available devices,” *Eye Brain*, vol. 10, pp. 13–24, Feb. 2018. doi: 10.2147/EB.S148644.

- [15] J. Rosen, B. Hannaford, and R. M. Satava, Eds., *Surgical Robotics: Systems Applications and Visions*. New York: Springer-Verlag, 2011, pp. 226–229.
- [16] P. Rahimian and J. K. Kearney, “Optimal camera placement for motion capture systems,” *IEEE Trans. Vis. Comput. Graph.*, vol. 23, no. 3, pp. 1209–1221, 2016. doi: 10.1109/TVCG.2016.2637334.
- [17] A. J. Petruska and J. J. Abbott, “Optimal permanent-magnet geometries for dipole field approximation,” *IEEE Trans. Magn.*, vol. 49, no. 2, pp. 811–819, 2013. doi: 10.1109/TMAG.2012.2205014.
- [18] B. Siciliano, L. Sciavicco, L. Villani, and G. Oriolo, *Robotics: Modeling, Planning and Control*. New York: Springer-Verlag, 2010.
- [19] C. M. Heunis, Y. P. Wotte, G. Phillips Furtado, J. Sikorski, and S. Misra, “The ARMM system—Autonomous steering of magnetically-actuated catheters: Towards endovascular applications,” *IEEE Robot. Autom. Lett.*, vol. 5, no. 2, pp. 704–711, 2020. doi: 10.1109/LRA.2020.2965077.
- [20] G. v. d. Bergen, “A fast and robust GJK implementation for collision detection of convex objects,” *J. Graph. Tools*, vol. 4, no. 2, pp. 7–25, 1999. doi: 10.1080/10867651.1999.10487502.
- [21] X. Yang, W. Yang, H. Zhang, H. Chang, C.-Y. Chen, and S. Zhang, “A new method for robot path planning based artificial potential field,” in *Proc. IEEE Conf. Industrial Electronics and Applications (ICIEA)*, Hefei, China, June 2016, pp. 1294–1299. doi: 10.1109/ICIEA.2016.7603784.
- [22] Y. Zhang and L. Jin, *Robot Manipulator Redundancy Resolution*. Hoboken, NJ: Wiley, 2017.
- [23] Y. Zhang, Z. Li, and H.-Z. Tan, “Inequality-based manipulator-obstacle avoidance using the LVI-based primal-dual neural network,” in *Proc. IEEE Int. Conf. Robotics and Biomimetics (ROBIO)*, Kunming, China, Dec. 2006, pp. 1459–1464. doi: 10.1109/ROBIO.2006.340144.

**Christoff M. Heunis**, Surgical Robotics Laboratory, Department of Biomechanical Engineering, University of Twente, The Netherlands. Email: c.m.heunis@utwente.nl.

**Beatriz Farola Barata**, Surgical Robotics Laboratory, Department of Biomechanical Engineering, University of Twente, The Netherlands. Email: beatriz.barata@kuleuven.be.

**Guilherme Phillips Furtado**, Surgical Robotics Laboratory, Department of Biomechanical Engineering, University of Twente, The Netherlands. Email: g.phillipsfurtado@utwente.nl

**Sarthak Misra**, Surgical Robotics Laboratory, Department of Biomechanical Engineering, University of Twente, The Netherlands; Department of Biomedical Engineering, University of Groningen and University Medical Centre Groningen, The Netherlands. Email: s.misra@utwente.nl.

BR